Research Square

Preprints are preliminary reports that have not undergone peer review.
They should not be considered conclusive, used to inform clinical practice,
or referenced by the media as validated information.

A Wearable Closed-Loop Insulin Micropump toward a Miniaturized Artificial Pancreas for Diabetes

Xinyu Xue

xuexinyu@uestc.edu.cn

University of Electronic Science and Technology of China https://orcid.org/0000-0003-1379-6813

Ziyu Kuang

University of Electronic Science and Technology of China

Xiangbin Kong

University of Electronic Science and Technology of China

Tan Cao

University of Electronic Science and Technology of China

Rui Lin

University of Electronic Science and Technology of China

Zhihe LONG

University of Electronic Science and Technology of China https://orcid.org/0000-0003-3815-2029

Tianyou Jiang

University of Electronic Science and Technology of China

Xianchun Jin

University of Electronic Science and Technology of China

Zhangzhi Zhao

University of Electronic Science and Technology of China

Meihua Chen

Sichuan Cancer Hospital & Institute, Sichuan Cancer Center, University of Electronic Science and Technology of China

Article

Keywords:

Posted Date: July 15th, 2026

DOI: https://doi.org/10.21203/rs.3.rs-10049534/v1

License: This work is licensed under a Creative Commons Attribution 4.0 International License.
Read Full License

Additional Declarations: There is no conflict of interest

Version of Record: A version of this preprint was published at Microsystems & Nanoengineering on September 29th, 2026. See the published version at https://doi.org/10.1038/s41378-026-01463-2.

Abstract

The application of a fully autonomous artificial pancreas faces fundamental constraints from the bulky mechanical drives of conventional insulin pumps and the spatially separated glucose sensing unit. Herein, we report a wearable closed-loop insulin micropump that enables a miniaturized artificial pancreas for diabetes treatment. It seamlessly integrates an electrochemical micropump with an optical glucose-responsive microneedle (MN) sensor. The core actuation module features a novel semi-dry sandwich electrode configuration combined with a highly elastic latex membrane and a groove-type epoxy sealing architecture. This structural paradigm shift effectively eliminates bulk fluid flow and ensures robust hermeticity for precise, electrolysis-gas-driven, microliter-scale dosing with a precision of 0.5 μL. For continuous glucose monitoring, a polyvinylpyrrolidone/polyvinyl alcohol (PVP/PVA) hydrogel MN array functionalized with 9-anthracene boronic acid (9-ANB) is employed. The specific binding of interstitial glucose triggers measurable fluorescence quenching, which is precisely digitized by an integrated XYZ true-color sensor (detection range: 0-600 mg/dL). Comprehensive in vitro and in vivo evaluations demonstrate the platform's predictable, programmable delivery kinetics and excellent biocompatibility. In type 1 diabetic mouse models, a smartphone-controlled system by autonomously and effectively suppressed postprandial glycemic spikes, maintaining glycemic fluctuations within 25 mg/dL. This highly integrated, miniaturized design offers a compelling paradigm shift for next-generation, patient-friendly diabetes management systems.

One-Sentence Summary

A miniaturized, wireless artificial pancreas combining an electrochemical micropump and an optical microneedle sensor delivers autonomous, closed-loop glycemic regulation.

Introduction

Diabetes mellitus is one of the most significant global healthcare challenges of the 21st century [1, 2]. According to the International Diabetes Federation (IDF), an estimated 589 million adults worldwide are living with diabetes, a figure projected to surge to 853 million by 2050 [3, 4]. The chronic nature of the disease, characterized by persistent hyperglycemia, leads to severe long-term complications including cardiovascular disease, nephropathy, and retinopathy, necessitating precise and rigorous glycemic control [5-7]. Exogenous insulin replacement therapy via continuous subcutaneous insulin infusion (CSII) has historically been the cornerstone of therapeutic management for insulin-dependent patients [8, 9]. In recent years, the clinical paradigm has rapidly evolved to Automated Insulin Delivery (AID) and Advanced Hybrid Closed-Loop (AHCL) systems [10-12]. These systems like artificial pancreases integrate continuous glucose monitoring (CGM) devices with algorithm-driven insulin pumps to automatically adjust basal rates and precisely deliver correction boluses, achieving superior glycemic control and significantly increasing the time within target blood glucose ranges for patients [13-15].

Despite these clinical triumphs, the realization of a fully autonomous, highly integrated, and patient-friendly artificial pancreas remains hindered by the fundamental architectures of current commercial devices [16-18]. Existing wearable insulin pumps primarily employ mechanical or electromagnetic drive systems [19, 20]. The reliance on rigid, complex moving components in traditional drives usually results in bulky, energy-intensive, and conspicuous devices [21, 22]. These inherent drawbacks frequently compromise patient comfort, ultimately leading to premature abandonment of the device [23]. To overcome the dimensional limits of mechanical drives, electrochemical micropumps offer a promising solution for the miniaturized artificial pancreas [24, 25]. Electrochemical, electrolysis-gas-driven actuation provides notable advantages for drug delivery, including high energy density, precise microliter-scale dosing, and the elimination of complex mechanical gears [26, 27]. Furthermore, the sensing component in current AID systems typically functions as a spatially separated unit [28, 29]. Emerging microneedle (MN) technology, based on fluorescent hydrogels for interstitial fluid (ISF) analysis, has shown great promise for painless, tether-free glucose monitoring via continuous fluorescence quenching mechanisms [30-32]. Thus, a single, miniaturized theranostic platform could potentially be achieved by seamlessly integrating optical glucose sensors with reliable electrochemical actuation modules [33-35].

Herein, we present a wearable closed-loop insulin micropump that enables a miniaturized artificial pancreas in diabetes therapy. The ultra-compact, intelligent theranostic platform integrates a novel electrochemical micropump with a glucose-responsive MN sensor. The micropump features a synergistic combination of a robust dual-chamber sealing architecture and a semi-dry electrode configuration inspired by wick. Regulated by a wireless Bluetooth Low Energy (BLE) control circuit, the applied current triggers water electrolysis, generating gases that drive the large-scale deformation of the latex membrane to extrude insulin. To close the therapeutic loop, a PVP/PVA hydrogel MN array infused with 9-anthracene boronic acid (9-ANB) is integrated for glucose detection. Upon extracting interstitial fluid (ISF), the selective binding of glucose to 9-ANB triggers measurable fluorescence quenching, which is precisely digitized by an onboard XYZ true-color sensor, providing high-resolution detecting without the enzymatic instability typical of electrochemical biosensors. Comprehensive experimental evaluations demonstrate the highly predictable dosing kinetics of this platform. The programmable flexibility allows the smartphone-operated system to switch seamlessly between a stable "basal" rate for long-term glycemic maintenance and rapid, high-dose "bolus" injections. By integrating highly stable sensing with multidimensional, customizable actuation, this platform provides a novel strategy for developing next-generation wearable artificial pancreas systems.

Results and Discussion

Design of closed-loop insulin micropump

To realize autonomous glycemic regulation in a user-friendly and highly compact form factor, we design an intelligent closed-loop theranostic platform. It seamlessly integrates an electrochemical insulin micropump with a glucose monitoring unit. A diabetic patient wearing this miniaturized device can

continuously monitor subcutaneous glucose levels and execute personalized therapeutic interventions, including single high/low dose, sustained release, or personalized dose via a custom smartphone application (**Figure 1a**).

The structural blueprint of the system features a spatially optimized, dual-chamber architecture (**Figure 1b**). The top compartment houses the custom-designed control circuit and the electrolysis chamber. The electrolysis chamber contains the highly porous nickel foam electrodes. The bottom compartment serves as the drug reservoir. Beneath the bottom compartment, a glucose-responsive MN array is attached and makes direct contact with the skin. The middle layer houses the optical sensing module and the circuit. The micropump employs a highly elastic latex membrane as a flexible piston to strictly isolate the actuation chamber from the drug reservoir. The hermetic integrity is further reinforced by a dedicated groove-type structure filled with epoxy resin. A flexible printed circuit (FPC) bridges the top control module with the bottom optical sensing module.

The closed-loop operational mechanism of the device is driven by real-time optical feedback (**Figure 1c**). Upon sensing a hyperglycemic state, the smartphone wirelessly commands the microcontroller unit (MCU) to output a precise constant current. This triggers water electrolysis within the nickel foam electrodes, generating gas that expands the latex membrane to extrude insulin into the subcutaneous tissue. Concurrently, the bottom sensor continuously captures the fluorescence quenching signals from the MN array, transmitting the digitized glucose data back to the smartphone to close the theranostic loop.

The integration of the electronics is critical for the device's miniaturization (**Figure 1d-f**). The circular segment of the FPC integrates a Bluetooth Low Energy (BLE) communication module, a constant current generator, and power interfaces, with electrode connection pads located on its reverse side. The rectangular extension contains the optical sensing components, including a UV LED and an XYZ true-color sensor (**Figure S1-S2**). Due to the exceptional mechanical flexibility of the FPC (**Figure 1e**), it can be conformally folded and wrapped around the cylindrical pump body. Optical photographs of the assembled device (**Figure 1g-j**) demonstrate the compact appearance and small size of the fully integrated wearable artificial pancreas. Both its outer diameter and thickness are both approximately 2 cm, highlighting its significant potential for unobtrusive, long-term clinical deployment. As shown in **Figure S3**, our closed-loop insulin micropump with the integrated sensing unit is much smaller than the commercial insulin pump and CGM device.

Mechanism of closed-loop theranostic

To achieve autonomous glycemic regulation, we devised a closed-loop feedback workflow integrating the MN sensor and an electrochemical micropump (**Figure 2a**). In operational mode, the sensing module continuously measures glucose concentration fluctuations within the subcutaneous interstitial fluid. A UV LED excites the microneedles to generate optical signals, which are captured by an integrated miniature XYZ true-color sensor. The signals are wirelessly transmitted to a smartphone via the Bluetooth module within the micro-control circuit for real-time processing and evaluation. Upon

detecting a hyperglycemic state, the control circuit is activated to output a constant current for a specified duration, driving the electrodes inside the micropump to electrolyze water and generate gas. The resulting pneumatic pressure causes the deformation of the highly elastic latex membrane, thereby enabling precise drug delivery. As the blood glucose level gradually returns to baseline, the system automatically suspends drug delivery. Thus, an intelligent theranostic loop without manual intervention is established.

The fundamental mechanism underlying the system's highly reliable delivery, lies in the dynamic deformation and displacement of the highly elastic latex membrane within the micropump. As illustrated in the photographs and cross-sectional schematics (**Figures 2b-2c**), the continuous generation of electrolytic gas causes the latex membrane to expand as a flexible piston. It continuously extrudes the drug solution from a filled state to an empty state without leakage. Mechanical tensile testing reveals that the latex membrane exhibits exceptional elasticity, accommodating a strain of nearly 700% (**Figure 2d**), which guarantees structural integrity and fatigue resistance during prolonged fluid displacement. A ultra-thin polyvinylidene chloride (PVDC) layer is also uniformly coated onto the membrane surface to ensure hermeticity (**Figure S4-S5**)(**Supplementary Note 1**). Furthermore, the output kinetics of the micropump demonstrate high predictability. Under a constant driving current, the experimentally measured cumulative volume exhibits a high degree of alignment with the theoretical volume variation curve (**Figure 2e**)(**Supplementary Note 2**), confirming the reliability of this electrochemical pneumatic mechanism for precise, microliter-scale dosing control.

For continuous glucose sensing, we employed a glucose-responsive MN array functionalized with 9-ANB (**Figure 2f**). The photograph displays the well-defined MN array structure, while the inset demonstrates the patch's excellent mechanical flexibility, ensuring conformal adhesion to human skin. Spectroscopic characterization validates its excellent optical properties (**Figure 2i**). Under 365 nm UV excitation, the emission spectrum of the 9-ANB exhibits a sharp characteristic peak in the blue light region. In practical observation, the MN array emits bright blue fluorescence upon UV irradiation before exposure to glucose (**Figure 2g**). After absorbing a glucose-containing solution, the formation of boronate esters through the binding of glucose to 9-ANB alters the electronic structure and vibrational characteristics of the fluorophore, subsequently inducing a pronounced and reversible fluorescence quenching effect (**Figure 2h**) [36, 37]. This purely optical intensity-based mechanism circumvents the chronic issues of enzyme degradation and electron mediator leakage typical of traditional electrochemical biosensors [38, 39]. It lays a solid sensing foundation for long-term, stable in vivo CGM [40].

Electrochemical actuation and delivery kinetics

To achieve highly efficient and miniaturized pneumatic actuation, we engineer a semi-dry sandwich electrode architecture. It comprises two highly porous nickel foam electrodes clamping a layer of non-woven fabric pre-saturated with NaOH electrolyte. The overall thickness is only approximately 2 mm (**Figure 3a**). This unique configuration maximizes the active electrochemical surface area while localizing the electrolyte, thereby driving gas expansion for drug displacement while mitigating leakage

risks. Meanwhile, it features high shape-customizability, allowing the internal layout to be tailored, which facilitates significant device miniaturization. Compared to traditional planar interdigitated electrodes, the nickel foam design exhibits significantly enhanced electrochemical kinetics. As illustrated in the I-V curves (**Figure 3b**), the nickel foam electrode demonstrates a markedly lower onset voltage for gas generation and produces a substantially higher current magnitude at equivalent voltages. Furthermore, under prolonged constant-voltage electrolysis, the nickel foam architecture maintains superior current stability, mitigating the rapid performance degradation typically observed in interdigitated configurations (**Figure 3c**).

Reliable therapeutic actuation necessitates precise electronic regulation and rigorous thermal management. The custom-designed micro-control circuit delivers a stable constant current output over a continuous timeframe (**Figure 3d**), ensuring predictable electrolytic gas generation. Meanwhile, infrared thermography illustrates the internal and external temperature distribution of the device after 60 seconds of operation (**Figure 3e**). The peak temperatures of the pump's external surface adjacent to the skin, as well as the internal electrode surface undergoing the electrolysis reaction, reach only 29.4 °C. This mild thermal footprint falls well within safe physiological limits, ensuring continuous patient comfort and preventing any thermal damage to adjacent skin tissue. It also ensures that the properties of the drug within the pump's reservoir are not compromised during wearable applications.

To visually demonstrate the drug release process, the micropump, driven by the integrated control circuit, was loaded with distinct model drugs (methyl orange, rhodamine B, and methylene blue). They are successfully injected into a biomimetic gelatin skin model (**Figure 3f**). The pumping kinetics are highly tunable and programmable. Experimental evaluations indicate a robust, predictable correlation between the drug infusion rate and the magnitude of the applied control current (**Figure 3g**). Moreover, device-to-device consistency is significant for clinical translation. Across five independently fabricated pump units, the cumulative delivered volume shows favorable linearity and minimal standard deviation under continuous 20 mA and 30 mA constant current driving (**Figure 3h**). Real-time monitoring of the output dynamics further confirms a smooth infusion rate with an extremely low fluctuation range under both current conditions (**Figure 3i**). Finally, the long-term operational reliability of the integrated actuation module was validated. After 20 days of storage, the drug volume dispensed during a standard 3-minute electrolysis cycle remained largely consistent with the initial baseline across multiple devices (**Figure 3j**). The results show the exceptional shelf-life and dependability of this electrochemical platform for chronic disease management.

Glucose-sensing microneedles

To enable continuous and minimally invasive extraction of interstitial fluid (ISF) for precise glucose monitoring, a polymeric MN array was applied as a sensing interface. The MN array was fabricated via a multi-step, vacuum-assisted micromolding technique (**Figure 4a**). Initially, a precursor solution comprising polyvinyl alcohol (PVA), polyvinylpyrrolidone (PVP), and the fluorescent monomer 9-ANB (PPA) was cast into a polydimethylsiloxane (PDMS) mold. Following vacuum treatment and drying at 35

°C to form the active sensing tips, a pure PVA solution was introduced into the mold as the backing layer. A subsequent round of vacuuming and complete drying enabled demolding of the integrated MN array. PVP possesses hydrophilicity and high mechanical strength, enabling the MN tips to rapidly absorb ISF and providing sufficient hardness to penetrate the stratum corneum. PVA exhibits good fluorescence enhancement properties along with high flexibility. As a backing layer, it allows for conformable adhesion to the skin. Macroscopically, the MN array exhibits high optical transparency (**Figure 4b**), an advantageous property for the efficient transmission of internal UV excitation and the resulting fluorescent emission signals. Scanning electron microscopy (SEM) characterization reveals a highly uniform and precisely defined conical morphology across the array (**Figure 4c**). The magnified view of a single microneedle demonstrates a sharp tip profile (**Figure 4d**), which is a critical geometric feature for ensuring efficient and painless penetration of the stratum corneum.

For reliable wearable applications, the MN array must possess dual physical properties: robust mechanical strength for skin insertion and superior hydrophilicity for rapid ISF extraction. Mechanical compression testing (**Figure 4g**) demonstrates that the MN array can withstand substantial applied force before failure, with a maximum compressive strength of approximately 10 N. This result indicates a mechanical integrity that satisfies the requirements for reliable epidermal penetration. Furthermore, the fluid extraction kinetics were evaluated using a rhodamine B solution model. The time-dependent spectrum (**Figure 4i**) reveals a rapid and progressive increase in red fluorescence intensity over a 20-minute absorption period. This confirms the good swelling capability of the PVA/PVP hydrogel matrix, which ensures a continuous and stable influx of ISF to the embedded fluorophores.

The core sensing mechanism of the platform relies on the specific binding between glucose and the boronic acid moieties of 9-ANB, which induces a pronounced fluorescence quenching effect. This phenomenon is visually confirmed in the PPA precursor solution mixed with glucose (**Figure 4h**). The intensity of the blue fluorescence under continuous UV excitation progressively diminishes as the glucose concentration increases. Upon integration with a miniaturized XYZ true-color sensor, the optical response of the hydrated MN array was quantitatively digitized in real time. As indicated by the sensor readouts (**Figure 4e**), the X (red) and Y (green) channel responses remained relatively insensitive to glucose fluctuations. The Z-axis response exhibited a significant and continuous decline, which specifically corresponds to the blue light emission band. Crucially, within typical physiological and pathological ranges, isolating the Z-axis value reveals a highly robust linear correlation ($R^2 = 0.995$) between the blue light intensity and glucose concentration (Figure 4f). This excellent linearity and specificity effectively translate chemical binding events into clear digital optical signals, establishing a solid foundation for the autonomous operation of the integrated closed-loop system.

In vivo closed-loop theranostic evaluation

To evaluate the practical clinical potential of the integrated wireless closed-loop theranostic platform, comprehensive in vivo experiments were conducted using mouse models. The miniaturized device could be conformally and securely attached to the dorsal skin of the mice, demonstrating excellent wearability

(**Figure 5a**). The minimal invasiveness and biological safety of the MN array are critical prerequisites for continuous tissue interfacing. Upon removal of the MN patch, the microscopic punctures on the stratum corneum almost completely disappeared within 15 minutes, indicating rapid and non-scarring skin recovery (**Figure 5c**).

Following safety validation, the closed-loop therapeutic efficacy of the platform was systematically investigated in type 1 diabetic mouse models. The in vivo experiment was divided into four groups: the Blank group consisted of non-diabetic mice, and the other three groups comprised STZ-induced type 1 diabetic mice. After a 12-hour fasting period, a commercial blood glucose sensor was utilized to continuously monitor the blood glucose levels of the four groups over the subsequent12 hours. Mouse tail venous blood was collected at 1-hour intervals to measure blood glucose. During this period, all four groups were fed initially, and the food was removed after the mice had eaten. Upon detecting the hyperglycemic state, the Micropump group was treated using our device, with a smartphone application wirelessly triggering via Bluetooth to execute a 15-second programmed insulin delivery. For comparison, the Blank and Control groups received physiological saline via traditional subcutaneous injection. The Manual group received a standard subcutaneous injection of a 60 μL insulin solution containing a 0.05 mg dose. This dose is widely established in literature as a safe control benchmark with no risk of overdose. The in vivo pharmacokinetic profiles (**Figure 5d**) reveal that the therapy administered by the device effectively suppressed the glycemic spike and maintained blood glucose within a steady target range. The therapeutic efficacy of the Micropump group matches the Manual group. By enabling highly precise, automated microliter-scale dosing, the intelligent system effectively avoided the risks of severe hypoglycemia, showcasing its significant potential as a next-generation autonomous diabetes management solution.

Concurrent with therapeutic intervention, the in vivo continuous glucose monitoring capability of the system was rigorously verified. Once inserted into the subcutaneous tissue, the MN array exhibited bright blue fluorescence under 365 nm UV excitation (**Figure 5b**). Subsequently, we quantified the real-time optical sensing performance across eight mice. The integrated color sensor wirelessly transmitted data to a smartphone application. Governed by the specific binding between glucose and the 9-ANB fluorophore, an elevated glucose concentration induces a pronounced fluorescence quenching effect. The in vivo sensor readouts (**Figure 5e**) illustrate this dynamic response under different physiological conditions. During the fasting state, blood glucose remained relatively low, yielding a consistently high Z-axis value (blue light). In stark contrast, during the feeding state, the postprandial blood glucose significantly attenuated the Z-axis value. This robust inverse correlation confirms the system's capacity to reliably track physiological blood glucose fluctuations in complex living systems.

To evaluate the minimally invasive nature of the microneedle (MN) array and the self-healing kinetics of the skin barrier, a detailed histopathological analysis of the puncture sites on mouse skin was performed via hematoxylin and eosin (H&E) staining (**Figure 5f**). Immediately upon MN removal (0 min), only microchannels formed by the mechanical compression of the microneedles were observed in the epidermis, without any severe tissue tearing, hemorrhage, or deep structural disruption. At 20 and 40 min

post-removal, these microchannels exhibited a rapid closure and self-healing tendency, with localized skin depression significantly reduced. The epidermal structure had substantially recovered its integrity. Furthermore, elucidating the immunogenicity and biocompatibility of the MN delivery system in vivo is paramount for its wearable clinical translation. To this end, multiplex immunofluorescence staining was employed to track the recruitment and polarization states of macrophages in mouse skin tissues over an extended period (Days 0, 2, and 4) following MN withdrawal (**Figure 5g**). In this evaluation, dual staining was performed using CD68 (red fluorescence) as a pan-macrophage marker and CD206 (green fluorescence) as an M2 (reparative) macrophage marker. Quantitative histological characterization revealed that CD68-positive cells (total macrophages) around the punctured region did not undergo explosive accumulation, but rather decreased progressively over the 5-day observation period (**Figure S6**). This result indicated that the hydrogel matrix did not trigger severe acute or chronic foreign body reactions. Concurrently, indicators of immune perturbation naturally subsided, exhibiting negligible localized immune activation. It confirmed the excellent biocompatibility of the PVA/PVP hydrogel matrix during sustained epidermal penetration.

Conclusion

The realization of a truly autonomous and unobtrusive artificial pancreas has long been hindered by the bulky, rigid mechanical drives of commercial insulin pumps and the physically separated glucose sensing unit. In this study, we bridge this engineering gap using an ultra-compact, wireless theranostic platform that synergizes a 9-ANB-functionalized optical microneedle sensor with a structurally novel electrochemical micropump. By engineering a unique semi-dry sandwich electrode that uses highly porous nickel foam to clamp a localized NaOH-saturated fabric, the system achieves highly efficient electrolytic actuation via predictable gas expansion. This structural paradigm shift enables arbitrary internal layout customization, shrinking the integrated device to overall dimensions of approximately 2 cm in diameter and thickness. Furthermore, the synergistic integration of the actuation module with the optically responsive microneedle array establishes a highly robust closed-loop theranostic cycle. By continuously translating glucose-dependent fluorescence variations into precise dosing commands via a smartphone interface, the platform achieves highly predictable, microliter-scale intervention. In vivo validation confirmed its capability to rapidly stabilize glycemic excursions while intrinsically safeguarding against severe hypoglycemia. This ultra-compact and wireless paradigm transcends the dimensional limitations of traditional devices, providing a viable, patient-friendly blueprint for the future of personalized diabetes care.

Method

Design of the Flexible Printed Circuit

A customized FPC was engineered to govern the fully autonomous closed-loop theranostic workflow. The master control unit was built upon a highly integrated Bluetooth Low Energy (BLE) microcontroller (HJ-531IMF V1.0) for reliable wireless data transmission. An onboard programmable constant current

source was constructed using an LT3092 linear current regulator, which was paired with an N-channel MOSFET (DMN1260UFA-7B) to enable precise Pulse Width Modulation (PWM) regulation of the electrolytic current. The integrated optical sensing module incorporated a UV LED (XL-1608UBC-04) for continuous fluorescence excitation, along with an I2C- interface XYZ true-color sensor (AS73211-AQFM) to continuously digitize the fluorescence quenching signals from the microneedle array. A low-dropout (LDO) voltage regulator (SSP7615-33DFR) was employed to maintain highly stable power delivery across the entire active system.

Fabrication of Semi-Dry Sandwich Electrode

A 1.0-mm-thick non-woven fabric was pre-soaked in a 10 wt% NaOH solution for 10 s to ensure complete and uniform electrolyte saturation. It was then tightly sandwiched between two layers of 0.5-mm-thick nickel foam. The inherent rough and highly porous microstructures of the nickel foam effectively interlocked with the fibrous network of the non-woven fabric. The assembled composite electrode was sectioned to a dimension of 1.0 cm × 1.0 cm, and conductive wires were soldered to the outer surfaces of both nickel foam layers.

Assembly of Dual-Chamber Micropump

The structural housings of both the electrolysis chamber and the drug reservoir were modeled using Shapr3D and manufactured via high-precision 3D printing. A highly elastic latex membrane (0.1 mm in thickness) was utilized as a flexible displacement piston. To ensure hermetic sealing, a 20-μm-thick polyvinylidene chloride (PVDC) layer was uniformly coated onto the membrane surface. During the device assembly, the top and bottom chambers were bonded with Nanda 705 silicone rubber. The groove architecture at the junction of the two chambers was filled with epoxy resin.

Fabrication of Glucose-Responsive Microneedle Array

Initially, a 12 wt% polyvinyl alcohol (PVA) solution was prepared. The PVA powder was dissolved in a water bath at 90 °C under continuous magnetic stirring at 200 rpm for approximately 2 hours until a uniform and viscous solution was formed. After cooling to room temperature, polyvinylpyrrolidone (PVP) powder was added at a PVP-to-PVA mass ratio of 3:4. The mixture was continuously stirred at 200 rpm for another 2 hours to achieve complete dissolution, resulting in a transparent hydrogel precursor solution. Separately, a 0.02 M 9-anthracene boronic acid (9-ANB) solution was prepared in 52% (v/v) ethanol. The hydrogel solution and the 9-ANB solution were then mixed at a 1:1 volume ratio and stirred at 200 rpm for approximately 1 hour to ensure homogeneity. The resulting mixture was allowed to stand for about 10 minutes to naturally degas before being carefully cast into a polydimethylsiloxane (PDMS) micromold. To completely eliminate internal air bubbles and guarantee the full filling of the micromold cavities, a vacuum degassing treatment was applied. Following this, the mold was dried at 35 °C for 24 hours to form the solidified MN tips. Subsequently, a pure PVA solution was cast onto the back of the dried MN tips as the backing layer. A secondary vacuum and drying treatment was performed. Finally, the integrated sensing MN array was carefully demolded using tweezers.

Characterization and measurements

The absorption spectra of the materials were tested using a UV-Vis spectrophotometer (UV-5100, Metash). The fluorescence emission spectra were analyzed using a fluorescence spectrometer (Aqualog, Horiba). The tensile strength of the membrane was measured using a universal testing machine (INSTRON 5982). The mechanical strength of the microneedles was tested using a texture analyzer (FTC TMS-TOUCH). The microscopic morphology of the microneedles was characterized using a scanning electron microscope (SEM, Zeiss Gemini 300). The internal and external surface temperatures of the device were measured using an infrared thermal imager (HM-TPK20-3AQF/W, HIKVISION). Measurements related to voltage and current were conducted using a DC power supply (SP-305, A-BF). A micropump extension tube with an internal diameter of 2 mm was used to measure the output liquid volume of the device.

In Vivo Blood Glucose Regulation in Mice

A total of 20 mice were randomly allocated into four groups (5 mice per group): the Blank group, the Control group, the Manual injection group, and the Micropump therapy group. Mice in the Blank group were healthy, non-diabetic controls, whereas mice in the other three groups were subjected to streptozotocin (STZ) induction to establish type 1 diabetic mouse models. Prior to the formal intervention, the random blood glucose levels of all STZ-induced mice were monitored daily for 3 consecutive days. Mice with stable random blood glucose levels exceeding 16 mmol/L were deemed successful type 1 diabetic models and subsequently enrolled in the therapeutic evaluations. Prior to the formal administration evaluation, all mice across the four groups underwent a 12 h fasting period with free access to water. The entire blood glucose monitoring period lasted for 12 h, during which blood samples were collected from the tail vein at a fixed 1 h interval, and the blood glucose levels were quantified using a commercial blood glucose sensor. To simulate a postprandial glycemic spike, a quantified amount of food was provided to the four groups of mice at the beginning of the monitoring (t = 0 h). Immediately after the mice had finished feeding, all food was removed, and the mice were maintained under strict fasting conditions for the remainder of the 12 h monitoring period. Following the feeding phase, distinct therapeutic interventions were performed via subcutaneous injection (s.c.). Specifically, each mouse in the Blank and Control groups received 60 μL of sterile normal saline as a negative control. For the Manual injection group (positive control), a microsyringe was utilized to manually administer 60 μL of insulin solution containing a standard dose of 0.05 mg exogenous insulin per mouse. In the Micropump therapy group, controlled via a smartphone, the onboard circuit of our device output a constant current of 50 mA to implement a 15-second drug administration protocol. Upon completion of the 12 h glycemic pharmacokinetic monitoring, all experimental mice were returned to standard housing cages with free access to food and regular husbandry management restored.

In Vivo Glucose Sensing Characterization

For the in vivo blood glucose sensing characterization, a total of eight mice were utilized to evaluate and compare the glycemic profiles between a 12 h fasting state and an ad libitum feeding state. Ten minutes

after recording the baseline blood glucose levels using a reference commercial blood glucose meter, the integrated microneedle (MN) patch sensor was conformally attached to the dorsal skin surface of the mice. The onboard optical sensor captured the dynamic fluorescence intensity variations generated by the MN array upon absorbing subcutaneous interstitial fluid (ISF) containing distinct glucose concentrations. The digitized sensing data were subsequently transmitted wirelessly to a smartphone terminal in real time. By correlating and comparing these wireless optical sensor readouts with the reference blood glucose data simultaneously gathered by the commercial blood glucose meter, the in vivo blood glucose levels reflected by the wearable sensing platform could be quantitatively evaluated.

Skin Histological Staining and Image Analysis

To evaluate the tissue compatibility and safety of the microneedle array applied to the skin, hematoxylin and eosin (H&E) staining was performed on mouse skin tissues collected at different time points (0, 20, and 40 min) post-treatment. The excised skin tissues were fixed in formaldehyde, dehydrated through a graded ethanol series and cleared using an automated tissue processor (JT-12S, Wuhan Junjie Electronics), followed by paraffin wax embedding (BMJ-A, Changzhou Zhongwei). The paraffin-embedded tissue sections were dewaxed to water, stained with hematoxylin solution for 5-10 minutes, differentiated in hydrochloric acid-ethanol, blued in a weak alkaline aqueous solution, and subsequently stained with eosin solution for 3 minutes. Finally, the sections were dehydrated through graded ethanol, cleared, and mounted with neutral balsam. Histological images were captured using a slide scanning imaging system (SQS-600P, Shenzhen Shengqiang Technology) . This procedure was used to systematically observe the structural integrity of the epidermis, dermis, subcutaneous tissue, and muscle layers, thereby assessing the time-dependent recovery of minor localized lesions such as tissue depression, microabscesses, and hyperchromatic nuclei of epidermal spinous cells at the puncture sites.

Multiplex Immunofluorescence Staining and Image Analysis

To evaluate the localized immune and foreign body responses following microneedle insertion, multiplex immunofluorescence staining was performed on mouse skin sections to analyze macrophage recruitment and polarization (using CD68 as a pan-macrophage marker and CD206 as an M2 macrophage marker). Paraffin-embedded sections were dewaxed in xylene, rehydrated through a graded ethanol series, and subjected to microwave-assisted antigen retrieval in a citrate buffer. Subsequently, endogenous peroxidase activity was quenched with 3% hydrogen peroxide, and non-specific binding was blocked with 3% bovine serum albumin (BSA) at room temperature. To achieve double labeling, the sections were first incubated with the initial primary antibody overnight at 4 °C, followed by an HRP-conjugated secondary antibody, and then subjected to tyramide signal amplification (TSA) using a TYR-520PLUS fluorescent dye. After a second microwave treatment to strip the initial non-covalently bound antibody complexes, the sections were incubated with the second primary antibody (overnight at 4 °C) and subsequently with a fluorophore-conjugated secondary antibody (CY3-conjugated goat anti-rabbit). Finally, cell nuclei were counterstained with DAPI, and the slides were mounted using an anti-fluorescence quenching medium. Multi-channel fluorescence images (CD68 in red, CD206 in green, and

nuclei in blue) were acquired using a whole-slide scanning system (VS200, Olympus), and the quantitative analysis of fluorescence-positive cells at different observation time points was performed using Image-Pro Plus software (Media Cybernetics).

Ethical statement

All animal experiments and procedures conducted in this study were performed in strict accordance with the relevant laws, regulations, and institutional guidelines for the care and use of laboratory animals. The experimental protocols were formally reviewed and approved by the Ethics Committee of Sichuan Cancer Hospital (Approval Number: SCCHEC-04-2023-026). Throughout all in vivo experimental periods, the mice were housed in a standardized, controlled environment under a 12 h light/12 h dark cycle at a maintained room temperature of 21 ± 2 °C, with ad libitum access to a standard laboratory diet and water.

Declarations

Acknowledgments:

Funding: This work was supported by Sichuan Science and Technology Program (grant nos. 2024NSFSC0143 to X.X. and 2024YFFK0333 to L.X.) and the Precision Radiation in Oncology Key Laboratory of Sichuan Province (grant no. 2024ROKF06 to L.X.).

Author contributions:

Conceptualization: Z.K., T.C., Z.L., X.X., and M.C.

Methodology: Z.K., X.K., T.C., R.L., Z.L., T.J., X.J., X.X., and M.C.

Investigation: Z.K., X.K., T.C., R.L., Z.L., X.X., and M.C.

Visualization: Z.K., X.K., T.J., and X.X.

Funding acquisition: X.X., Z.Z., and M.C.

Project administration: X.X. and M.C.

Supervision: X.X. and M.C.

Writing - original draft: Z.K.

Writing - review & editing: Z.K., X.K., X.X., and M.C.

Conflict of interest: The authors declare no competing interests.

Ethical declaration: Ethics approval and informed consent were obtained from all participants and the protocol approved by the Ethics Committee for Medical Research and New Medical Technology of Sichuan Cancer Hospital (SCCHEC-04-2023-026).

Data and materials availability: All data needed to evaluate the conclusions in this paper are present in the paper or the Supplementary Materials.

References

[1] Zheng Y, Ley S H, Hu F B. Global aetiology and epidemiology of type 2 diabetes mellitus and its complications[J]. Nature reviews endocrinology, 14(2): 88-98 (2018).

[2] Saeedi P, Petersohn I, Salpea P, et al. Global and regional diabetes prevalence estimates for 2019 and projections for 2030 and 2045: Results from the International Diabetes Federation Diabetes Atlas[J]. Diabetes research and clinical practice, 157: 107843 (2019).

[3] Sun H, Saeedi P, Karuranga S, et al. IDF Diabetes Atlas: Global, regional and country-level diabetes prevalence estimates for 2021 and projections for 2045[J]. Diabetes research and clinical practice, 183: 109119 (2022).

[4] Cho N H, Shaw J E, Karuranga S, et al. IDF Diabetes Atlas: Global estimates of diabetes prevalence for 2017 and projections for 2045[J]. Diabetes research and clinical practice, 138: 271-281 (2018).

[5] Diabetes Control and Complications Trial Research Group. The effect of intensive treatment of diabetes on the development and progression of long-term complications in insulin-dependent diabetes mellitus[J]. New England journal of medicine, 329(14): 977-986 (1993).

[6] Nathan D M, DCCT/Edic Research Group. The diabetes control and complications trial/epidemiology of diabetes interventions and complications study at 30 years: overview[J]. Diabetes care, 37(1): 9-16 (2014).

[7] Harding J L, Pavkov M E, Magliano D J, et al. Global trends in diabetes complications: a review of current evidence[J]. Diabetologia, 62(1): 3-16 (2019).

[8] JC P. Continuous subcutaneous insulin infusion at 25 years[J]. Diabetes Care, 25(3): 593-598 (2002).

[9] Yeh H C, Brown T T, Maruthur N, et al. Comparative effectiveness and safety of methods of insulin delivery and glucose monitoring for diabetes mellitus: a systematic review and meta-analysis[J]. Annals of internal medicine, 157(5): 336-347 (2012).

[10] Bekiari E, Kitsios K, Thabit H, et al. Artificial pancreas treatment for outpatients with type 1 diabetes: systematic review and meta-analysis[J]. bmj, 361 (2018).

[11] Weisman A, Bai J W, Cardinez M, et al. Effect of artificial pancreas systems on glycaemic control in patients with type 1 diabetes: a systematic review and meta-analysis of outpatient randomised controlled trials[J]. The lancet Diabetes & endocrinology, 5(7): 501-512 (2017).

[12] Kovatchev B. A century of diabetes technology: signals, models, and artificial pancreas control[J]. Trends in Endocrinology & Metabolism, 30(7): 432-444 (2019).

[13] Brown S A, Kovatchev B P, Raghinaru D, et al. Six-month randomized, multicenter trial of closed-loop control in type 1 diabetes[J]. New England Journal of Medicine, 381(18): 1707-1717 (2019).

[14] Bergenstal R M, Garg S, Weinzimer S A, et al. Safety of a hybrid closed-loop insulin delivery system in patients with type 1 diabetes[J]. Jama, 316(13): 1407-1408 (2016).

[15] Battelino T, Danne T, Bergenstal R M, et al. Clinical targets for continuous glucose monitoring data interpretation: recommendations from the international consensus on time in range[J]. Diabetes care, 42(8): 1593-1603 (2019).

[16] Cobelli C, Renard E, Kovatchev B. Artificial pancreas: past, present, future[J]. Diabetes, 60(11): 2672-2682 (2011).

[17] Lal R A, Ekhlaspour L, Hood K, et al. Realizing a closed-loop (artificial pancreas) system for the treatment of type 1 diabetes[J]. Endocrine reviews, 40(6): 1521-1546 (2019).

[18] Trevitt S, Simpson S, Wood A. Artificial pancreas device systems for the closed-loop control of type 1 diabetes: what systems are in development?[J]. Journal of diabetes science and technology, 10(3): 714-723 (2016).

[19] Thabit H, Hovorka R. Continuous subcutaneous insulin infusion therapy and multiple daily insulin injections in type 1 diabetes mellitus: a comparative overview and future horizons[J]. Expert Opinion on Drug Delivery, 13(3): 389-400 (2016).

[20] Boughton C K, Hovorka R. New closed-loop insulin systems[J]. Diabetologia, 64(5): 1007-1015 (2021).

[21] Garg S K, Weinzimer S A, Tamborlane W V, et al. Glucose outcomes with the in-home use of a hybrid closed-loop insulin delivery system in adolescents and adults with type 1 diabetes[J]. Diabetes technology & therapeutics, 19(3): 155-163 (2017).

[22] Tanenbaum M L, Hanes S J, Miller K M, et al. Diabetes device use in adults with type 1 diabetes: barriers to uptake and potential intervention targets[J]. Diabetes care, 40(2): 181-187 (2017).

[23] Lawton J, Blackburn M, Allen J, et al. Patients' and caregivers' experiences of using continuous glucose monitoring to support diabetes self-management: qualitative study[J]. BMC endocrine disorders, 18(1): 12 (2018).

[24] Noushin T, Parvez M S, Biswas P, et al. MEMS in Twenty-First-Century Healthcare[M]//Micro-and Nano-Systems in 21st-Century: Designs, Developments, Applications and Perspective. Singapore: Springer Nature Singapore: 71-132 (2025).

[25] Nisar A, Afzulpurkar N, Mahaisavariya B, et al. MEMS-based micropumps in drug delivery and biomedical applications[J]. Sensors and Actuators B: Chemical, 130(2): 917-942 (2008).

[26] Bhattacharjee N, Urrios A, Kang S, et al. The upcoming 3D-printing revolution in microfluidics[J]. Lab on a Chip, 16(10): 1720-1742 (2016).

[27] Meng E, Hoang T. Micro-and nano-fabricated implantable drug-delivery systems[J]. Therapeutic delivery, 3(12): 1457-1467 (2012).

[28] Heller A, Feldman B. Electrochemical glucose sensors and their applications in diabetes management[J]. Chemical reviews, 108(7): 2482-2505 (2008).

[29] Wang J. Electrochemical glucose biosensors[J]. Chemical reviews, 108(2): 814-825 (2008).

[30] Prausnitz M R. Engineering microneedle patches for vaccination and drug delivery to skin[J]. Annual review of chemical and biomolecular engineering, 8: 177-200 (2017).

[31] Yu J, Zhang Y, Ye Y, et al. Microneedle-array patches loaded with hypoxia-sensitive vesicles provide fast glucose-responsive insulin delivery[J]. Proceedings of the National Academy of Sciences, 112(27): 8260-8265 (2015).

[32] Wu Q, Wang L, Yu H, et al. Organization of glucose-responsive systems and their properties[J]. Chemical reviews, 111(12): 7855-7875 (2011).

[33] Lee H, Choi T K, Lee Y B, et al. A graphene-based electrochemical device with thermoresponsive microneedles for diabetes monitoring and therapy[J]. Nature nanotechnology, 11(6): 566-572 (2016).

[34] Kim J, Campbell A S, de Ávila B E F, et al. Wearable biosensors for healthcare monitoring[J]. Nature biotechnology, 37(4): 389-406 (2019).

[35] Heikenfeld J, Jajack A, Rogers J, et al. Wearable sensors: modalities, challenges, and prospects[J]. Lab on a Chip, 18(2): 217-248 (2018).

[36] Yoon J, Czarnik A W. Fluorescent chemosensors of carbohydrates. A means of chemically communicating the binding of polyols in water based on chelation-enhanced quenching[J]. Journal of the American Chemical Society, 114(14): 5874-5875 (1992).

[37] Wu Q, Wang L, Yu H, et al. Organization of glucose-responsive systems and their properties[J]. Chemical reviews, 111(12): 7855-7875 (2011).

[38] Shibata H, Heo Y J, Okitsu T, et al. Injectable hydrogel microbeads for fluorescence-based in vivo continuous glucose monitoring[J]. Proceedings of the National Academy of Sciences, 107(42): 17894-17898 (2010).

[39] Guan Y, Zhang Y. Boronic acid-containing hydrogels: synthesis and their applications[J]. Chemical Society Reviews, 42(20): 8106-8121 (2013).

[40] Heo Y J, Shibata H, Okitsu T, et al. Long-term in vivo glucose monitoring using fluorescent hydrogel fibers[J]. Proceedings of the National Academy of Sciences, 108(33): 13399-13403 (2011).

Figures

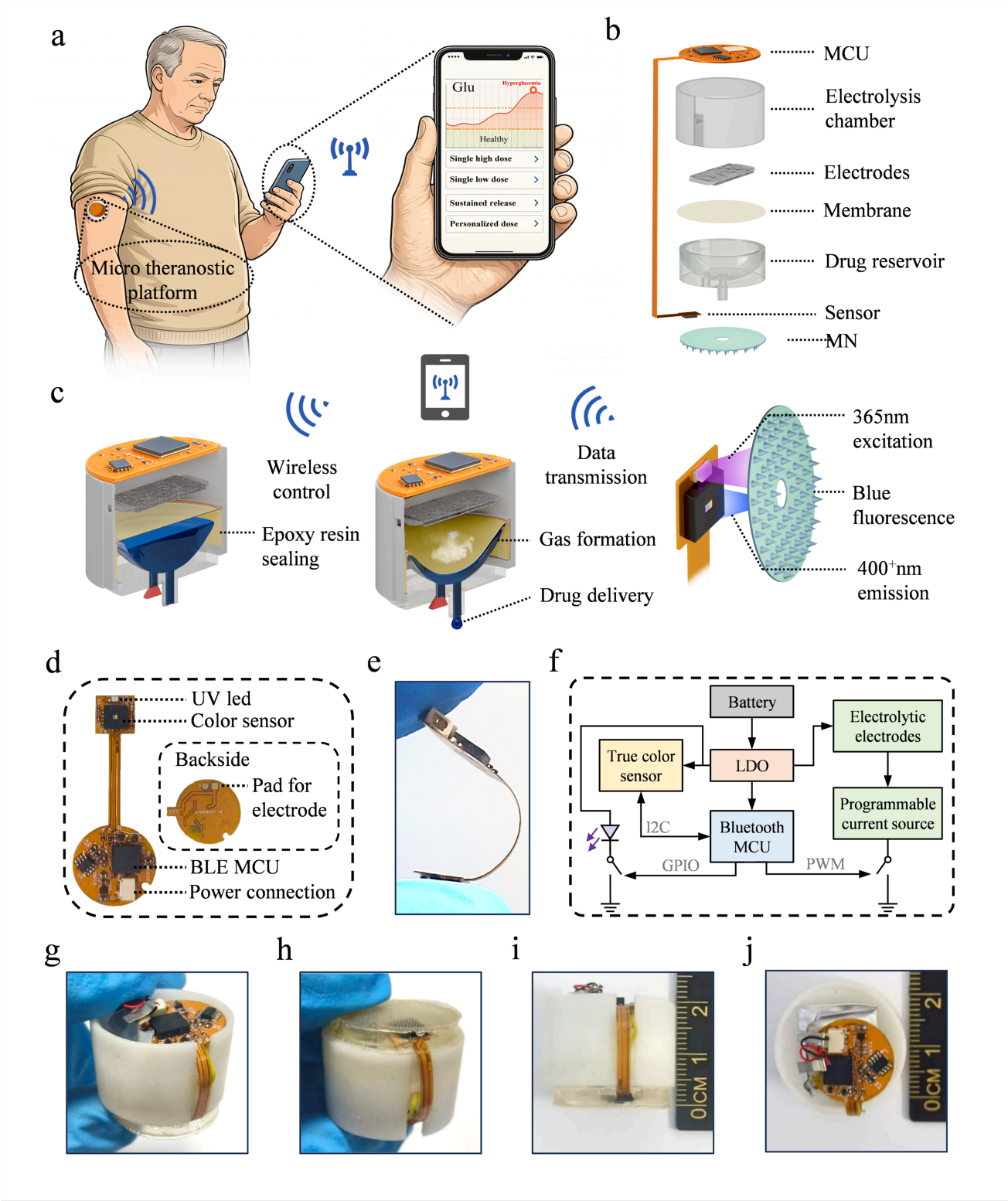


Figure 1

Design of closed-loop insulin micropump. (**a**) Concept of a patient wearing the insulin micropump for smartphone-controlled real-time closed-loop theranostics. (**b-c**) Exploded 3D view and closed-loop principle, detailing the dual-chamber structure, gas-driven insulin extrusion, and synchronized fluorescence glucose sensing. (**d-f**) Layout details, mechanical flexibility, and block diagram of the

flexible printed circuit (FPC). (**g-j**) Optical photographs of the fully assembled device from various angles, highlighting its extreme compactness

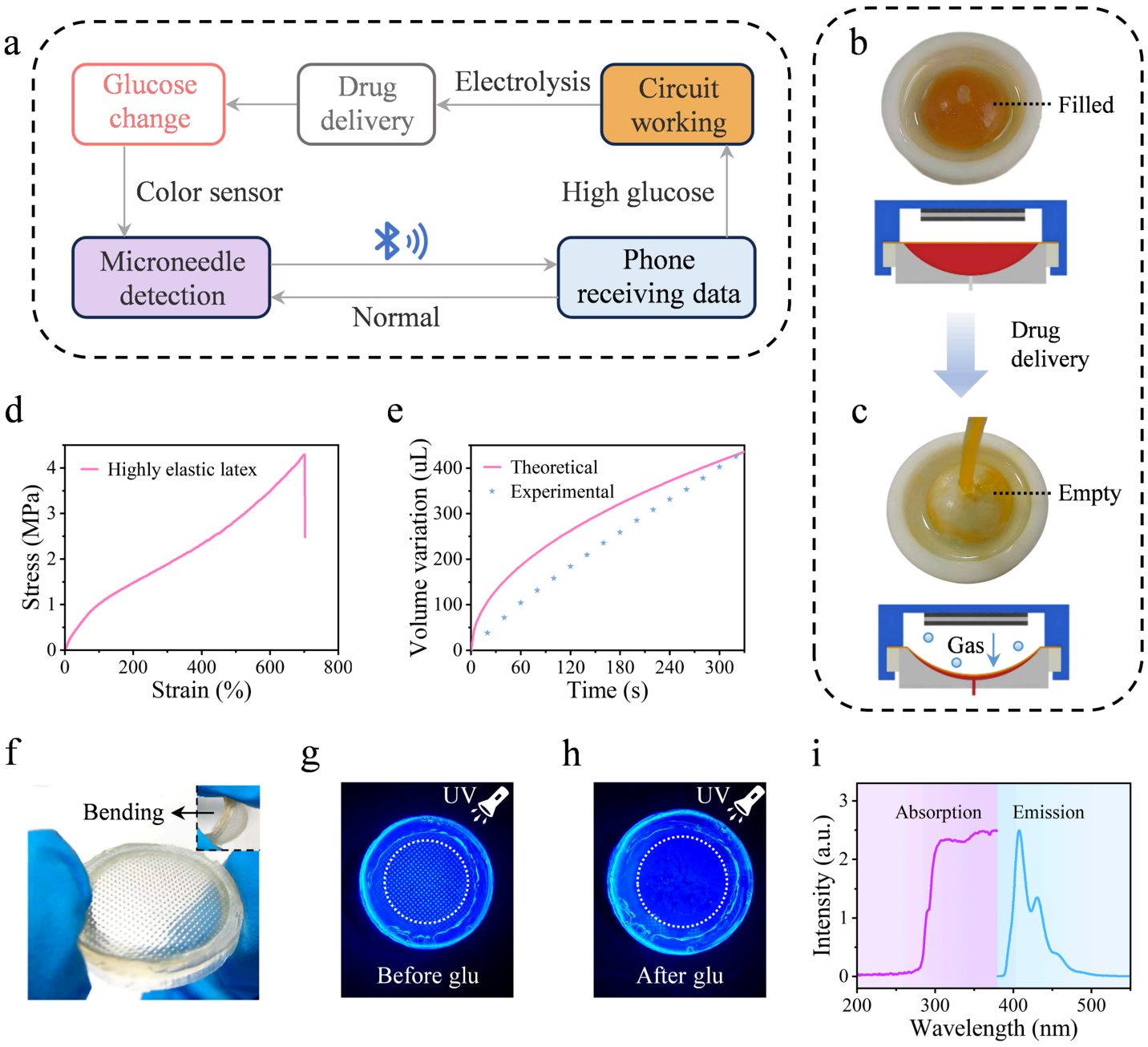


Figure 2

Mechanism of closed-loop theranostic. (**a**) Workflow of MN sensing and micropump delivery. (**b-c**) Photographs and cross-sections of the micropump in "Filled" and "Empty" states, showing gas-driven membrane deformation. (**d**) Stress-strain curve of the latex membrane. (**e**) Experimental and theoretical extruded volume under constant current. (**f**) Photograph of the flexible glucose-responsive MN. (**g-h**) MN

blue fluorescence before glucose exposure and distinct quenching after exposure. (**i**) UV-Vis absorption and emission spectra of the 9-ANB material.

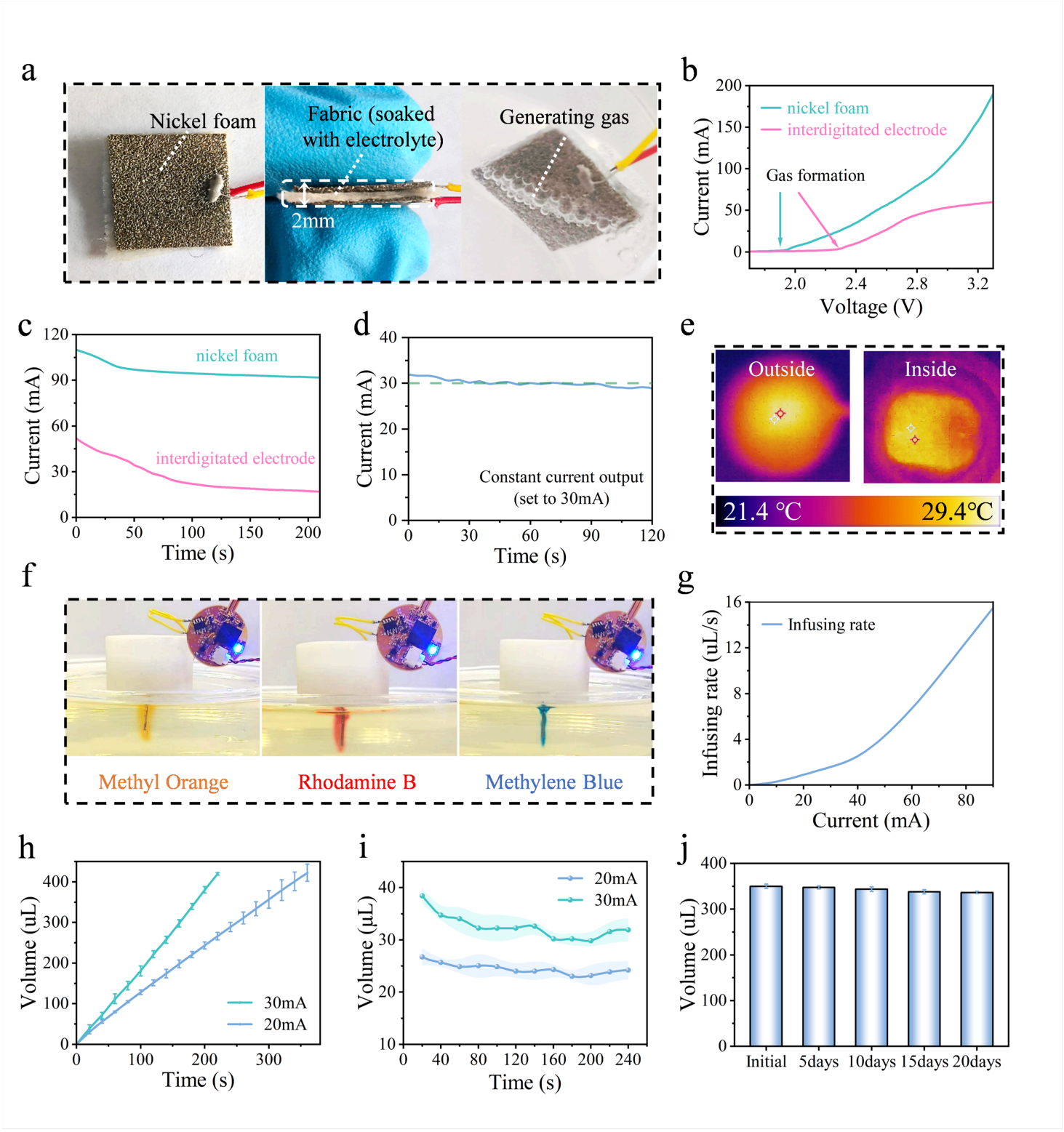


Figure 3

Electrochemical actuation and delivery kinetics. (**a**) Optical images of the 2-mm-thick sandwich electrode and gas generation. (**b-c**) I-V characteristics and chronoamperometric stability of nickel foam

versus interdigitated electrodes. (**d**) Stable 30 mA current output from the control circuit. (**e**) Infrared thermograms after 60 s of operation (peak at 29.4 °C). (**f**) Circuit-driven release of model drugs into a gelatin model. (**g**) Correlation between infusing rate and control current. (**h-i**) Cumulative volume and dynamic infusing rate measured every 20 s of five micropumps under 20 and 30 mA. (**j**) Output volume consistency of five micropumps after 0-20 days of storage.

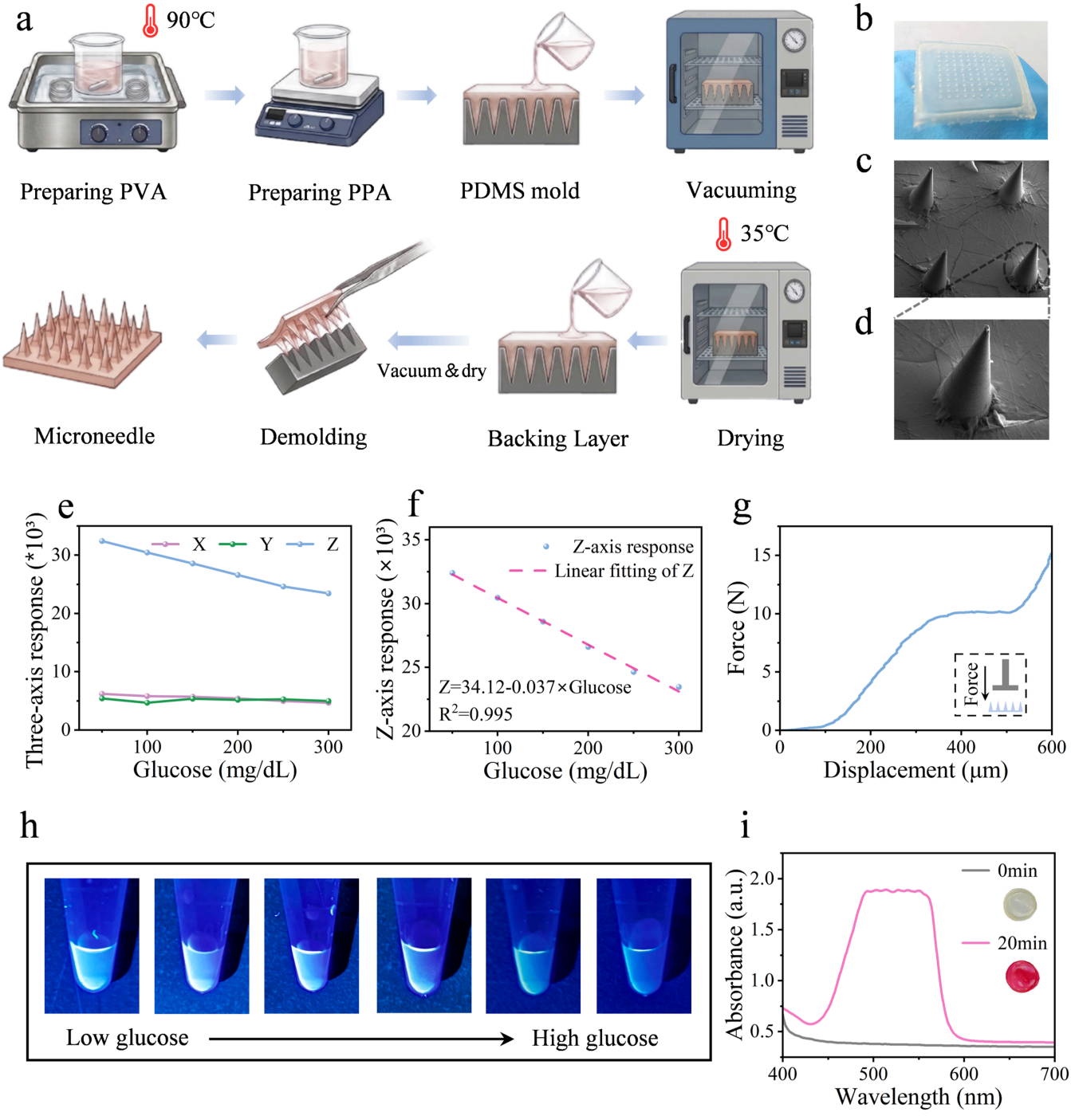


Figure 4

Glucose-sensing microneedles. (**a**) Fabrication process scheme. (**b**) Macroscopic and (**c-d**) SEM images of the PPA hydrogel MNs. (**e**) XYZ true-color sensor responses to varying glucose concentrations under UV excitation. (**f**) the corresponding Z-axis linear fitting curve (R^2 = 0.995). (**g**) Compressive force-displacement curve. (**h**) UV-irradiated PPA solutions showing glucose-dependent fluorescence quenching. (**i**) Fluorescence spectra of MNs after absorbing rhodamine B for 0-20 min.

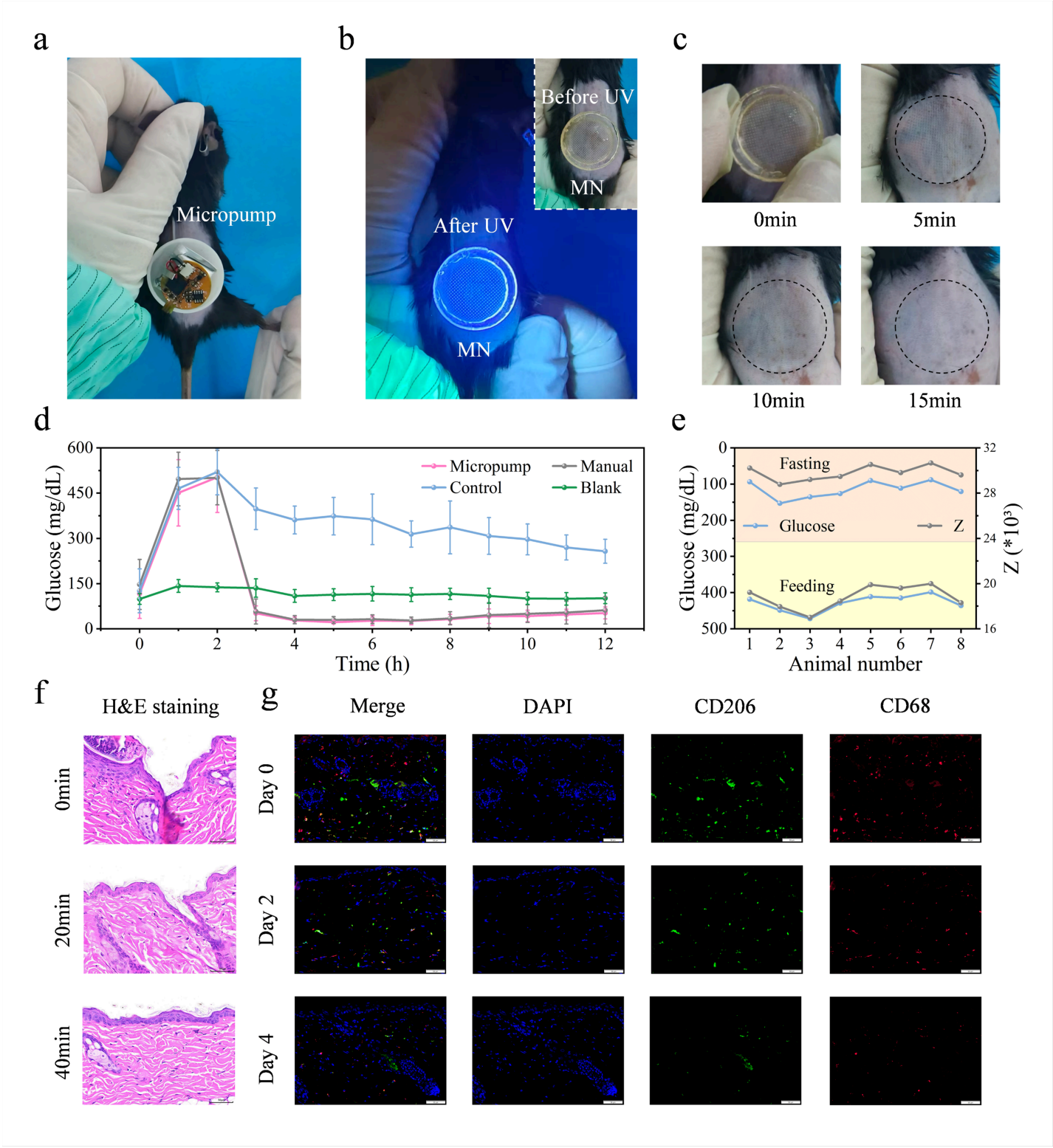


Figure 5

In vivo closed-loop theranostic evaluation (**a**) Device attached to a mouse. (**b**) Skin-adhered MN fluorescence under 365 nm UV (inset: pre-irradiation). (**c**) Skin recovery within 15 min post-removal. (**d**) 12-hour blood glucose profiles post-feeding for Blank, Control, Manual, and Micropump groups. (**e**) Continuous Z-axis (blue light) sensing data across 8 mice during Fasting and Feeding states. (**f**) H&E skin staining at 0,20, and 40 minutes post-MN insertion. (**g**) Immunofluorescence (DAPI/CD206/CD68) of skin on Days 0, 2, and 4 post-treatment.

Supplementary Files

This is a list of supplementary files associated with this preprint. Click to download.

- Supplementaryinformation.docx